Optics Letters

Characterization of rubidium thin cell properties with sandwiched structure using a multipath interferometer with an optical frequency comb

Sandan Wang,[1,2,†] Jinpeng Yuan,[1,2,†] Lirong Wang,[1,2,*] Liantuan Xiao,[1,2] and Suotang Jia[1,2]

[1]State Key Laboratory of Quantum Optics and Quantum Optics Devices, Institute of Laser Spectroscopy, Shanxi University, Taiyuan 030006, China
[2]Collaborative Innovation Center of Extreme Optics, Shanxi University, Taiyuan 030006, China
*Corresponding author: wlr@sxu.edu.cn

Received 19 July 2021; revised 13 August 2021; accepted 15 August 2021; posted 16 August 2021 (Doc. ID 438103); published 26 August 2021

The characterization of the layer properties of multilayered structures has attracted research interest owing to advanced applications in fields of atom-based sensors, ultra-narrow optical filters, and composite films. Here, a robust nondestructive multipath interferometry method is proposed to characterize the features of a thin cell with a borosilicate glass–rubidium–borosilicate glass sandwiched structure using a femtosecond optical frequency comb. The multipath interference method serves as a powerful tool for identification of the layer number and physical thickness of a three-layered structure. Moreover, the global distribution map is obtained by scanning the entire region. Furthermore, the amplitude of sub-Doppler reflection spectra of the rubidium D2 line is confirmed at different target points to validate this method. This result promotes the development of thin-cell-based atomic devices with strong light–matter interaction at atomic scales.

https://doi.org/10.1364/OL.438103

In recent years, multilayered structures have been used extensively in various fields, from atomic physics to stacked semiconductor devices [1–8]. The determination of the layer number and identification of each layer's physical properties are extremely decisive, not only in the manufacturing process, but also in practical applications. Among them, the thin cell with a substrate–alkali vapor–substrate sandwiched structure, in which the interaction with the laser radiation field is strictly anisotropic, is widely applied in the fields of magnetometry, optical filters, and optical clocks [9–13]. The precise thickness information identification of a thin vapor cell promises scalability and integrability for various applications in quantum information processing and communication [14–18].

Several methods are proposed to determine the layer properties of transparent materials with multilayered structures, including contact and noncontact measurements [19,20]. The contact method inevitably damages sample surfaces due to the use of a mechanical stylus, and it is difficult to inspect the thickness distribution in real time owing to slow measurement speed [21]. Among noncontact methods, ultrasonic wave inspection is an insensitive measurement because an additional propagation medium and harsh handling conditions are required [22]. The nondestructive inspections with x rays have to be considerate of shielding for safety because of the high photon energy [23].

Traditional optical interferometry [24,25] is also a nondestructive method for measuring optical thickness, but it induces undesired errors in the measurement process because additional measurement steps are needed to determine the refractive index [26–29]. A spectral domain interference method for characterizing a single-layered specimen is proposed [30]. Then, a multi-arm interferometer is constructed to achieve correction of the air refractive index to eliminate the effect of variations in environmental parameters [31]. Motivated by these previous methods, the characterization of the layer number and physical thickness of the multilayer structure is explored via a high-sensitivity multipath interferometer based on an optical frequency comb (OFC). This method can provide references for existing methods in the areas of thin films and low-emissivity windows.

In this Letter, we report the reproduction of the physical properties of a thin cell with a borosilicate glass–rubidium–borosilicate glass (BSG-rubidium-BSG) sandwiched structure using robust multipath interferometry based on a stabilized OFC. Three physical properties, the layer number, physical thickness, and refractive index of the BSG layer, are described with high precision via spectral analysis of multiple interference signals. The global distribution map of a thin cell is characterized by whole region dynamic scanning. Additionally, the sub-Doppler spectral profile of the rubidium D2 line at different target points of the thin cell is also explored to verify the measurement method. The direct determination of physical properties of a thin atomic cell, which is difficult to obtain, aids in the development of chip-scale atomic clocks and optical magnetometry.

The experimental setup to study the layer properties is composed of a measurement module and a test module, which is shown in Fig. 1(a). The OFC light source system (Menlo

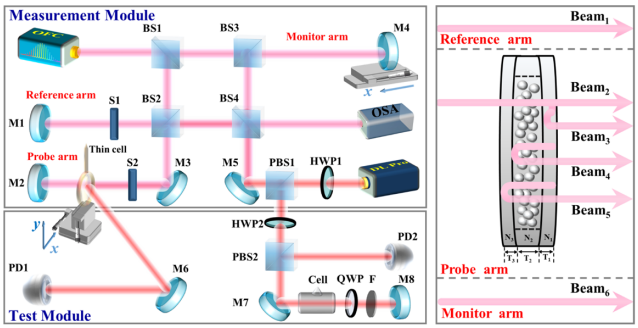

Fig. 1. (a) Experimental setup. OFC, optical frequency comb; M, reflection mirror; BS, beam splitter; S, shutter; OSA, optical spectrum analyzer; HWP, half-wave plate; PBS, polarizing beam splitter; QWP, quarter-wave plate; F, neutral density filter; PD, photodetector. (b) Schematic diagram of the multipath interference method.

systems, FC1500) for the measurement module operates at a center wavelength of 1560 nm with a full width at half maximum (FWHM) of approximately 60 nm. The diameter of the Gaussian beam is about 500 μm, and the output power is about 200 mW. The repletion rate f_{rep} is 250 MHz corresponding to a maximum non-ambiguity range $L_{\mathrm{NAR}} = c/(2f_{\mathrm{rep}}) = 0.6$ m, which is much larger than the interferometric distance. The laser delivered from the OFC is divided into three beams using beam splitters (BSs), which are injected into the reference, probe, and monitor arms. The introduction of an additional monitor arm can improve measurement accuracy by eliminating the influence of external environmental factors and laser power drift. Two shutters (S1 and S2) work alternately to construct two interferometers: the reference interferometer with reference and monitor arms, and the probe interferometer with probe and monitor arms. The thin cell is introduced into the probe arm, which is installed on an x-y linear motorized scanning stage with a travel range of 50 mm (x) × 50 mm (y). Additionally, the location of mirror M4 on the monitor arm is adjusted precisely using another linear translation stage, which induces pulse-to-pulse interference. An optical spectrum analyzer (OSA) (Yokogawa, AQ6370C) with a wavelength resolution of 0.02 nm is used to acquire the interference signal generated at BS4. Furthermore, the test module is fully spatial-coupled in the measurement module by using M5, BS4, and BS2 to evaluate the measurement results. The laser source is a 780 nm continuous-wave diode laser (Toptica, DL Pro), which is used to excite the Rb D2 line transition. The laser beam is split into two beams. The weaker beam is used to obtain the saturation absorption spectroscopy (SAS) in PD2 for frequency reference, and the stronger beam interacts with the thin vapor cell to obtain the sub-Doppler reflection spectra in PD1 carrying thickness information.

Figure 1(b) shows a schematic diagram of layer property measurements. Each layer of the thin cell has a physical thickness of T_i and refractive index of N_i ($i = 1, 2, 3$). To determine physical properties of each layer, several optical path differences (OPDs) are required. The intensity I of the interference spectrum corresponding to an OPD L can be expressed as [32]

$$I(f, L) = I_0(f) \cdot \left\{1 + \cos\left(2\pi f \frac{L}{c}\right)\right\} = I_0(f) \cdot \{1 + \cos\varphi(f, L)\}, \quad (1)$$

where $I_0(f)$ is the intensity of the light source, f is the optical frequency, and $\varphi(f, L)$ is the phase to be measured. To get the phase information corresponding to the OPD, only the peak located in the time domain is selected with a sampling window, and then is inverse-Fourier transformed. The phase is extracted by taking the imaginary part of the logarithmic function of the inverse-Fourier transform result. Finally, L can be determined by the phase slope $d\varphi/df$ obtained by the linear fit of $\varphi(f, L)$ [33]:

$$L = \frac{c}{2\pi}\frac{d\varphi}{df}. \quad (2)$$

Furthermore, L_{m-n} is defined as the OPD of Beam$_m$ and Beam$_n$. In the case without a sample, the OPDs of the reference interferometer and probe interferometer are L_{1-6} and L_{2-6}, respectively, which induce the OPD between the reference and probe arms $L_1 = L_{1-6} - L_{2-6}$. $L_3 = L'_{1-6} - L'_{2-6}$ is used as the OPD between the reference and probe arms in the case with a sample. The refractive indices of two BSG layers are defined as N. The refractive index of the vacuum layer N_2 with a small amount of rubidium media is considered as the vacuum refractive index 1.00 in the laser field far away from the atom resonance transition without nonlinear effects [34]. The layer number i is recognized by the effective spectral peak number n of the probe interferometer in the case with a sample, $i = n - 1$. Precise identification of sample layers by the number of interference peaks is applicable to other types of multilayered samples with different layer numbers and different materials. For the measurement of thickness and refractive index, T_{total} is first obtained by OPDs of L_1, L_3, and L_{2-5} using Eq. (3). T_2 is measured using L_{2-4}, L_{2-3}, and N_2 by Eq. (4):

$$T_{\mathrm{total}} = \frac{L_{2-5}}{2} - L_3 + L_1, \quad (3)$$

$$T_2 = \frac{L_{2-4} - L_{2-3}}{2 \cdot N_2}. \quad (4)$$

Then, N is determined by T_2, N_2, and T_{total} using Eq. (5):

$$N = \frac{L_{2-5} - 2 \cdot N_2 \cdot T_2}{2 \cdot (T_{\mathrm{total}} - T_2)}. \quad (5)$$

Third, T_1 is calculated by L_{2-3} and N using Eq. (6):

$$T_1 = \frac{L_{2-3}}{2 \cdot N}. \quad (6)$$

Finally, T_3 is obtained using T_{total}, T_2, and T_1:

$$T_3 = T_{\mathrm{total}} - T_2 - T_1. \quad (7)$$

Taking a fixed point on the thin cell as the target point, Figs. 2(a) and 2(c) present the interference spectra of the reference interferometer and probe interferometer in the case of no sample, respectively. Figures 2(b) and 2(d) show the corresponding amplitude spectra in the Fourier domain. The insets are the obtained phase information corresponding to amplitude peaks A_1 and B_1. The OPDs of $L_{1-6} = 5359.61$ μm and $L_{2-6} = 4554.09$ μm are determined by the phase data according to Eq. (2). Therefore, the OPD of the measurement arm and probe arm $L_1 = 805.52$ μm is obtained.

With the thin cell introduced into the probe arm, the interference spectrum and Fourier transform amplitude spectrum

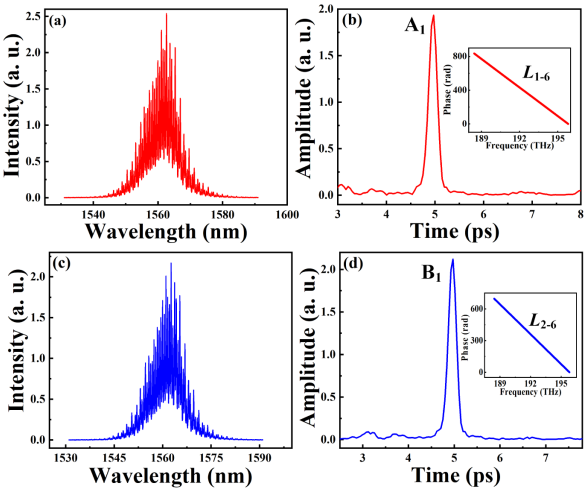

Fig. 2. (a) Interference spectrum and (b) Fourier transform amplitude spectrum of the reference interferometer obtained without a thin cell. (c) and (d) Cases of probe interferometer. Insets are the phase data corresponding to different amplitude spectra.

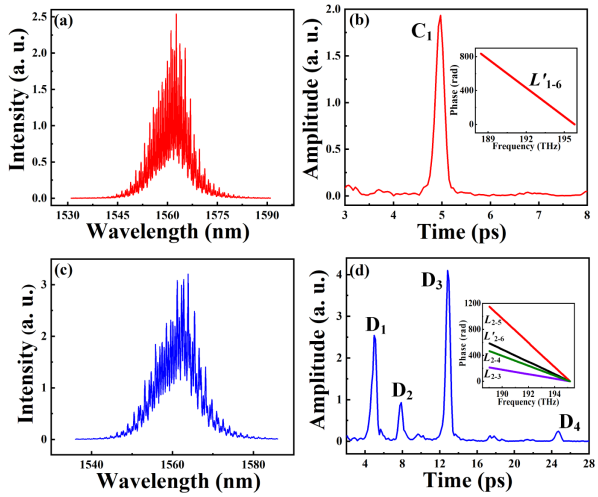

Fig. 3. (a) Interference spectrum and (b) corresponding Fourier transform amplitude spectrum of the reference interferometer obtained with a thin cell. (c) and (d) Cases of probe interferometer. Insets are phase data corresponding to different amplitude spectra.

of the reference interferometer are shown in Figs. 3(a) and 3(b). The case of the probe interferometer is shown in Figs. 3(c) and 3(d). Owing to multiple reflections of the multilayered structure surfaces, the enhanced stacking interference signal is observed in Fig. 3(c) compared to that in Fig. 3(a). The four main peaks, marked as D_1 to D_4, in Fig. 3(d) are distinguished clearly, which indicates a three-layered structure. The spectral peaks used to identify the layer number of the sample are distinguished by selective perturbation, such as disturbing the light source distribution, comparing the signals of the two interferometers, and blocking beam paths behind the sample. Other small unmarked peaks are caused by the distribution of the light source, its harmonics, and other undesired optical paths. The OPD of $L'_{1-6} = 5360.24\ \mu m$ is obtained in the inset of Fig. 3(b) from the C_1 peak. The OPDs of $L_{2-4} = 3779.07\ \mu m$, $L'_{2-6} = 3954.58\ \mu m$, $L_{2-3} = 1818.81\ \mu m$, and $L_{2-5} = 5701.33\ \mu m$ are characterized by the D_1, D_2, D_3, and D_4 peaks, respectively, in Fig. 3(d). Therefore, the physical thickness and refractive index, $T_2 = 979.87\ \mu m$, $N = 1.47$, $T_1 = 617.75\ \mu m$, and $T_3 = 652.89\ \mu m$, are extracted from the obtained OPDs using Eqs. (3)–(7).

During the measurement process, the main error source is the Fourier transform algorithm and the uncertainty of measurement repeatability. The measurement errors after the Fourier transform are less than 0.10 % when the OPD exceeds 1.0 mm [30], which suggests that the uncertainty of the Fourier transform is less than 3.04 μm. Uncertainty of measurement repeatability arises from the standard deviation of each OPD obtained by multiple repeated measurements, which is calculated to be approximately 2.73 μm. Additionally, the wavelength uncertainty comes from the wavelength accuracy of the OSA, which is given as 0.02 nm, and the uncertainty for the air refractive index is roughly 10^{-6}. The contribution to the uncertainty from these two uncertainty sources is around 50 nm. All in all, the entire experimental system suggests uncertainty of less than ~6.00 μm. Furthermore, adding more measuring arms can reduce the effect of external environmental factors and laser power drift, which will improve measurement accuracy.

The image of the thin cell with a BSG-rubidium-BSG sandwiched structure is shown in Fig. 4(a). Figure 4(b) shows the

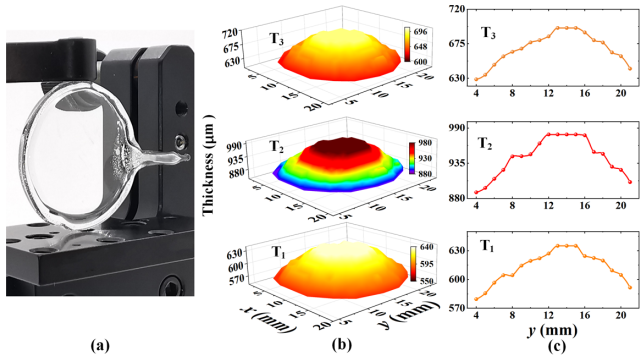

Fig. 4. (a) Image and (b) global thickness distribution maps of the thin cell with BSG-rubidium-BSG sandwiched structure. (c) Cross-section thickness profiles at $x = 15$ mm of each layer corresponding to (b).

global thickness distribution maps by dynamically scanning the entire region with a step of 1 mm. The thin edges and gradually thickened central structure are observed clearly. Furthermore, the relatively thin edges of the BSG substrate structure (T_1 and T_3) are induced by molten processing technology. The rubidium medium layer with different thicknesses (T_2), which indicate the different interaction lengths with the laser, directly determines the development of atom-based sensors and optical resonators [35,36]. The cross-section thickness profiles at $x = 15$ mm corresponding to Fig. 4(b) are shown in Fig. 4(c). It can be found that the positions of $y = 13$–15 mm are the ideal range of most atomic-based experiments, which have uniform atomic vapor distribution and a smooth laser incident window. The surface defects of materials can also be effectively characterized. Additionally, the refractive index of the BSG layers is uniformly distributed, and is approximately 1.47. The result is consistent with the value given by the factory inspection report.

The reflection spectra of the rubidium D2 line based on a thin vapor cell are measured in Fig. 5(a) to evaluate the above characterization results. Target points of different thicknesses are selected for verification of the interaction of photon and atom. The reflection spectra are obtained by detecting the beam

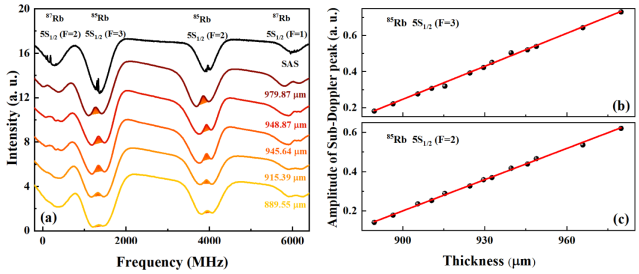

Fig. 5. (a) Reflection spectra at different target points of the thin cell. (b) and (c) Amplitudes of ^{85}Rb $5S_{1/2}(F=3)$ and ^{85}Rb $5S_{1/2}(F=2)$ sub-Doppler peaks as a function of rubidium layer thickness, respectively.

reflected from the second window of the thin vapor cell, which contributes to the formation of saturated absorption resonances centered at the hyperfine transitions [37]. Thus, the interaction length of the photon and atom is strongly dependent on the thickness of the thin cell, which determines the intensity of the reflected beam. The thickness information of the rubidium layer is reflected by the amplitude of sub-Doppler peaks. As shown in Fig. 5(a), we find that the well-expressed narrow sub-Doppler structures (red shadow) in the Doppler profiles are observed in reflection spectra of ^{85}Rb $5S_{1/2}(F=3)$ and ^{85}Rb $5S_{1/2}(F=2)$. The amplitude of ^{85}Rb $5S_{1/2}(F=3)$ and ^{85}Rb $5S_{1/2}(F=2)$ sub-Doppler peaks increase with the increase in rubidium layer thickness and show a linear relationship, which are shown in Figs. 5(b) and 5(c), respectively. The black dots represent the experimental results, and the red lines refer to the linear fitting results. The errors are the standard deviation of three measurements. The variation of the reflection spectrum with the thickness of the thin cell well credits the above interference measurement results.

In conclusion, we experimentally validated a method to measure the physical properties of a thin vapor cell with a BSG-rubidium-BSG sandwiched structure using nondestructive multipath interferometry. The multiple interference spectra with phase information are obtained to identify the layer number and physical thickness. Furthermore, the global distribution map is characterized by a thin edge and thick central structure. Additionally, the reflection spectra of the rubidium D2 line at different target points are obtained. The thickness information of the rubidium medium layer is clearly reflected by the amplitude of the sub-Doppler peak. The refractive index can also be identified by using the multipath interferometer for multilayer materials with the same refractive index information. This method can realize rapid real-time characterization of multilayered materials, which can be applied not only for the resulting description of devices but also for monitoring of the manufacturing process.

Funding. National Key Research and Development Program of China (2017YFA0304203); National Natural Science Foundation of China (61875112, 62075121, 91736209); Shanxi Provincial Key Research and Development Project (201803D421034); Program for Sanjin Scholars of Shanxi Province; 1331KSC.

Disclosures. The authors declare no conflicts of interest.

Data Availability. Data underlying the results presented in this paper are not publicly available at this time but may be obtained from the authors upon reasonable request.

[†]These authors contributed equally to this Letter.

REFERENCES

1. D.-H. Kim, J.-H. Ahn, W. M. Choi, H.-S. Kim, T.-H. Kim, J. Song, Y. Y. Huang, Z. Liu, C. Lu, and J. A. Rogers, Science **320**, 507 (2008).
2. Y. Lin, Y. Fang, J. Zhao, Y. Shao, S. J. Stuard, M. M. Nahid, H. Ade, Q. Wang, J. E. Shield, N. Zhou, A. M. Moran, and J. Huang, Nat. Commun. **10**, 1008 (2019).
3. C. Stehle, C. Zimmermann, and S. Slama, Nat. Phys. **10**, 937 (2014).
4. J. Yuan, S. Dong, C. Wu, L. Wang, L. Xiao, and S. Jia, Opt. Express **28**, 23820 (2020).
5. E. Vetsch, D. Reitz, G. Sagué, R. Schmidt, S. T. Dawkins, and A. Rauschenbeutel, Phys. Rev. Lett. **104**, 203603 (2010).
6. T. Xu, Y.-K. Wu, X. Luo, and L. J. Guo, Nat. Commun. **1**, 59 (2010).
7. Z. Zhang, F. Li, G. Malpuech, Y. Zhang, O. Bleu, S. Koniakhin, C. Li, Y. Zhang, M. Xiao, and D. D. Solnyshkov, Phys. Rev. Lett. **122**, 233905 (2019).
8. M. O. Araújo, H. L. D. de Souza Cavalcante, M. Oriá, M. Chevrollier, T. P. de Silans, R. Castro, and D. Moretti, Phys. Rev. A **88**, 063818 (2013).
9. D. K. Gramotnev and S. I. Bozhevolnyi, Nat. Photonics **4**, 83 (2010).
10. J. Yuan, S. Dong, H. Zhang, C. Wu, L. Wang, L. Xiao, and S. Jia, Opt. Express **29**, 2712 (2021).
11. B. Julsgaard, J. Sherson, J. I. Cirac, J. Fiurášek, and E. S. Polzik, Nature **432**, 482 (2004).
12. S. Wang, J. Yuan, L. Wang, L. Xiao, and S. Jia, Opt. Express **28**, 38334 (2020).
13. T. Udem, R. Holzwarth, and T. W. Hänsch, Nature **416**, 233 (2002).
14. F. Ripka, H. Kübler, R. Löw, and T. Pfau, Science **362**, 446 (2018).
15. H. Kübler, J. P. Shaffer, T. Baluktsian, R. Löw, and T. Pfau, Nat. Photonics **4**, 112 (2010).
16. H. Cai, J. Liu, J. Wu, Y. He, S.-Y. Zhu, J.-X. Zhang, and D.-W. Wang, Phys. Rev. Lett. **122**, 023601 (2019).
17. Z. Zhang, S. Liang, F. Li, S. Ning, Y. Li, G. Malpuech, Y. Zhang, M. Xiao, and D. Solnyshkov, Optica **7**, 455 (2020).
18. J. Sheng, U. Khadka, and M. Xiao, Phys. Rev. Lett. **109**, 223906 (2012).
19. A. Hirai and H. Matsumoto, Appl. Opt. **45**, 5614 (2006).
20. M. Haruna, M. Ohmi, T. Mitsuyama, H. Tajiri, H. Maruyama, and M. Hashimoto, Opt. Lett. **23**, 966 (1998).
21. J. Kim, H.-P. Ha, K.-M. Kim, and K.-Y. Jhang, Appl. Sci. **10**, 8661 (2020).
22. E. Moreno, P. Acevedo, and M. Castillo, Ultrasonics **37**, 595 (2000).
23. D. Pelliccia, A. Rack, M. Scheel, V. Cantelli, and D. M. Paganin, Phys. Rev. Lett. **117**, 219902 (2016).
24. V. Mazlin, P. Xiao, J. Scholler, K. Irsch, K. Grieve, M. Fink, and A. C. Boccara, Nat. Commun. **11**, 1868 (2020).
25. J. Große, M. Von Helversen, A. Koulas-Simos, M. Hermann, and S. Reitzenstein, APL Photon. **5**, 096107 (2020).
26. D. F. Murphy and D. A. Flavin, Appl. Opt. **39**, 4607 (2000).
27. H. Delbarre, C. Przygodzki, M. Tassou, and D. Boucher, Appl. Phys. B **70**, 45 (2000).
28. D. I. Farrant, J. W. Arkwright, P. S. Fairman, and R. P. Netterfield, Appl. Opt. **46**, 2863 (2007).
29. Q. D. Pham and Y. Hayasaki, Opt. Express **21**, 19003 (2013).
30. J. Jin, J. W. Kim, C.-S. Kang, J.-A. Kim, and T. B. Eom, Opt. Express **18**, 18339 (2010).
31. G. Wu, M. Takahashi, H. Inaba, and K. Minoshima, Opt. Lett. **38**, 2140 (2013).
32. H. Zhao, Z. Zhang, X. Xu, H. Zhang, J. Zhai, and H. Wu, Sensors **20**, 1743 (2020).
33. K.-N. Joo and S.-W. Kim, Opt. Express **14**, 5954 (2006).
34. J. Keaveney, I. G. Hughes, A. Sargsyan, D. Sarkisyan, and C. S. Adams, Phys. Rev. Lett. **109**, 233001 (2012).
35. D. J. Alton, N. P. Stern, T. Aoki, H. Lee, E. Ostby, K. J. Vahala, and H. J. Kimble, Nat. Phys. **7**, 159 (2011).
36. S. Knappe, P. Schwindt, V. Shah, L. Hollberg, J. Kitching, L. Liew, and J. Moreland, Opt. Express **13**, 1249 (2005).
37. S. Cartaleva, A. Krasteva, L. Moi, A. Sargsyan, D. Sarkisyan, D. Slavov, P. Todorov, and K. Vaseva, Quantum Electron. **43**, 875 (2013).